

Dynamic Background Reconstruction via MAE for Infrared Small Target Detection

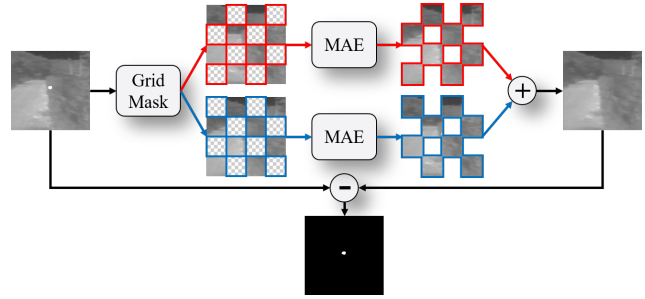
Jingchao Peng, Haitao Zhao, Kaijie Zhao, Zhongze Wang, and Lujian Yao
Automation Department, School of Information Science and Engineering,
East China University of Science and Technology

Abstract

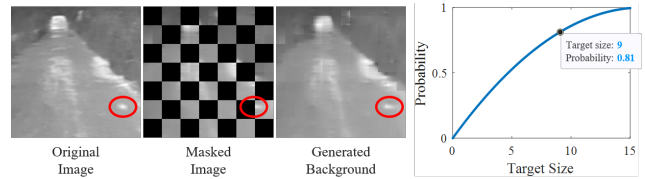
Infrared small target detection (ISTD) under complex backgrounds is a difficult problem, for the differences between targets and backgrounds are not easy to distinguish. Background reconstruction is one of the methods to deal with this problem. This paper proposes an ISTD method based on background reconstruction called Dynamic Background Reconstruction (DBR). DBR consists of three modules: a dynamic shift window module (DSW), a background reconstruction module (BR), and a detection head (DH). BR takes advantage of Vision Transformers in reconstructing missing patches and adopts a grid masking strategy with a masking ratio of 50% to reconstruct clean backgrounds without targets. To avoid dividing one target into two neighboring patches, resulting in reconstructing failure, DSW is performed before input embedding. DSW calculates offsets, according to which infrared images dynamically shift. To reduce False Positive (FP) cases caused by regarding reconstruction errors as targets, DH utilizes a structure of densely connected Transformer to further improve the detection performance. Experimental results show that DBR achieves the best F1-score on the two ISTD datasets, MFIRST (64.10%) and SIRST (75.01%).

1. Introduction

In recent years, infrared small-target detection (ISTD) is becoming more and more popular [5, 17, 30, 31]. Compared with visible light imaging, infrared imaging offers strong anti-interference, has the ability of long-range imaging, and can work around the clock [42]. Infrared imaging has been widely used in various fields, especially in intelligent robotics, autonomous driving, fire warning, agricultural production, leakage measurement, etc. [16, 27, 36, 42]. When the target is more than 10 kilometers away from the infrared detector, it usually occupies a small region (the target size is less than 9×9 pixels in 256×256 images [3]). In addition, due to atmospheric scattering and refraction,



(a) The structure of the naive background reconstruction method (NBR).



(b) Dividing one target into two patches will cause reconstruction failure. The probability of dividing one target into two patches at different target sizes

Figure 1. An ISTD method based on background reconstruction and its shortage.

optical defocusing, and various noises, infrared images have a low signal-to-noise (SNR) ratio and low contrast with the background [2]. These factors reduce the performance of ISTD methods, and thus ISTD is still a challenge in the field of target detection.

Due to extremely small sizes and low SNR ratio, targets in ISTD have inadequate detail information such as contour, shapes, textures, and so on, which is what visible light target detection methods rely on [24, 25, 27]. Therefore, most ISTD methods pay attention to differences between targets and backgrounds. For example, filter-based methods detect local gray differences between targets and backgrounds [15, 18]; human-visual-system-based (HVS) methods measure local contrast to detect targets [4, 9–11, 33]; deep-learning-based (DL-based) methods utilizing multiple nonlinear layers transform raw images into high-dimensional representations, in which targets and backgrounds have more significant differences than

in raw images [7, 14, 26, 29, 40, 41]. However, given complex backgrounds, the differences between targets and backgrounds are not easy to distinguish, resulting in poor detection performance. Consequently, detecting small targets under complex backgrounds is a difficult problem.

Clean backgrounds without targets can alleviate the detection problem under complex backgrounds [20]. Since targets do not belong to backgrounds, if the regions of the targets are masked, clean backgrounds can be obtained by image inpainting [39], whose purpose is to produce visually plausible structure and texture for the missing regions of images [35]. In the last few years, the success of Vision Transformers [8] has brought new opportunities to image inpainting. Vision Transformers embed one input image into 16×16 patches. Compared with convolutional neural networks, which process the whole feature map, Vision Transformers have natural advantages in integrating mask tokens into images. MAE [12] removes random patches to reconstruct pixels under a high masking ratio (75%) and works well. Therefore, the idea of masking patches with targets and reconstructing backgrounds via MAE naturally comes to us.

Inspired by MAE [12], we propose a naive background reconstruction method (NBR). NBR adopts a grid masking strategy and reconstructs one image twice with a masking ratio of 50%. Two mask patches compose a “mutually exclusive and collectively exhausting” (MECE) image. The structure of NBR can be shown in Fig. 1a. NBR assumes that masked backgrounds can be reconstructed while masked targets cannot. The principle is that given twice reconstruction with a masking ratio of 50%, the probability of the target being masked is 100%. So that NBR can reconstruct clean backgrounds without targets. However, when a target is divided into two neighboring patches, one-half of the target will be reconstructed based on the other half of the target, resulting in the failure of background reconstruction, as shown in Fig. 1b. Furthermore, when the target size is 9×9 , the probability of dividing one target into two patches is up to 81%. It is necessary for ISTD to avoid one target being divided into two neighboring patches.

The existing methods of avoiding dividing one target into two neighboring patches include enlarging the patch window [32, 37], adopting deformable embedding methods [34, 38], and shifting windows [19]. However, these methods are not designed for background reconstruction and cannot be directly used in ISTD. In specific, the methods of avoiding dividing one target into two neighboring patches, which can be used to reconstruct backgrounds, need to meet the following conditions:

- The same target can only be presented in one patch. Otherwise, the target will also be reconstructed.

- The principle of MECE must be satisfied between patches. Otherwise, the background will be reconstructed incompletely.

Therefore, it is necessary to design a special method for ISTD to avoid dividing one target into two patches.

Motivated by the above analysis, in this paper, we propose a background-reconstruction-based ISTD method called Dynamic Background Reconstruction (DBR), as shown in Fig. 2. DBR consists of a dynamic shift window module (DSW), a background reconstruction module (BR), and a detection head (DH). First, DSW calculates an offset base on how many pixels the target can move to the center of the patch in raw infrared images. Then, according to this offset, BR dynamically shifts windows before input embedding and uses NBR to reconstruct clean backgrounds. Finally, infrared images with targets, clean backgrounds without targets, and their difference are concatenated and fed into DH to improve the detection performance. Because the detector is prone to regard reconstruction errors as targets, the recall rate is greater than the precision rate. We propose a weighted dice loss (WDLoss) to balance the precision and recall rates.

In summary, our contributions are summarized below:

1. DBR is a background-reconstruction-based ISTD method that can improve detection performance under complex backgrounds. We propose a BR based on Vision Transformer (MAE) to reconstruct clean backgrounds without targets.
2. DBR can prevent the transformer from dividing one target into two neighboring patches, which is harmful to background reconstruction. We propose a DSW to calculate offsets, according to which BR dynamically shifts images before input embedding.
3. DBR is robust to reconstruction error. We propose a DH and a WDLoss, which can separately reduce the influence of reconstruction error on detection performance from aspects of the network architecture and loss function.

2. Related Works

In this section, we first summarize ISTD methods, including traditional and DL-based methods. Then we introduce existing vision transformers and how they avoid dividing one target into two patches.

2.1. Infrared Small-Target Detectio Methods

ISTD methods can be largely divided into traditional methods and deep learning-based methods [42]. Traditional methods utilize filters or the human visual system to detect targets, assuming the target is brighter than its neighbor

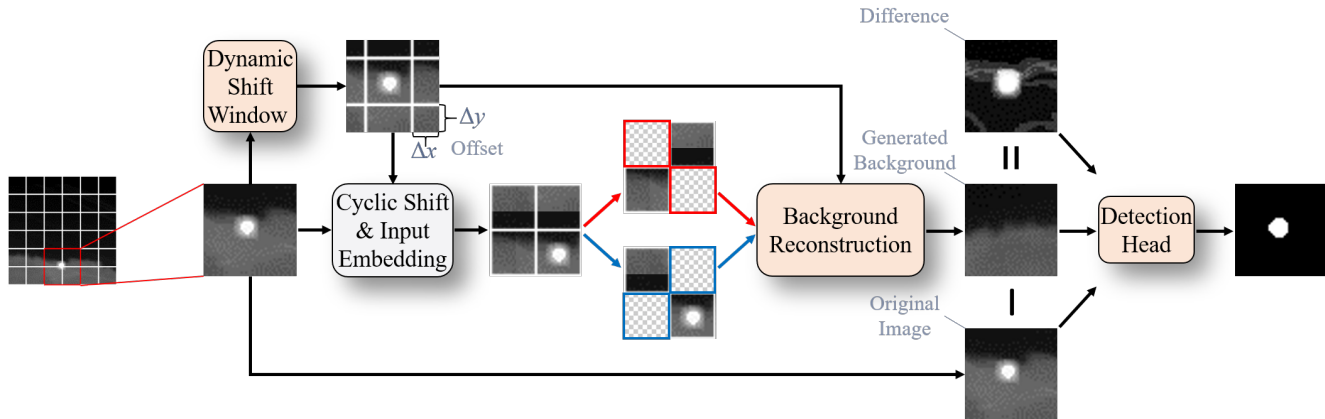


Figure 2. The architecture of the Dynamic Background Reconstruction method (DBR).

pixels. To strengthen the difference between targets and backgrounds, WSLCM [11] adopted a weighting function and strengthened LCM [4]; ADCDD [1] took advantage of local gray differences and employed weighting coefficients; ADMD [22] used directional information.

As for DL-based methods, due to small targets prone to disappear in forward propagation, the key technology is to enhance targets in complex backgrounds. For example, ACM [5] and ALCNet [6] utilized a bottom-up local attention module to transfer context information; IAANet [31] leveraged a transformer encoder to obtain interior relations between pixels; DNANet [17] proposed a dense nested attention network to maintain target information in deep layers; MDvsFA-cGAN [30] and CourtNet [23] utilized two subnetworks to separately enhance targets and suppress backgrounds. Existing ISTD methods rely on differences between targets and backgrounds to detect targets but cannot reconstruct clean backgrounds without targets.

2.2. Vision Transformers

MAE [12] developed an asymmetric encoder-decoder architecture, which masks random patches of the input image and reconstructs the missing pixels. The reconstruction performance is excellent when the masking ratio is less than 75%. However, since MAE uses a fixed input embedding method, which divides the image into 16×16 patches, targets are easily divided into two patches.

To avoid dividing one target into two patches, T2T-ViT [37] and PVT-V2 [32] utilized an overlapping patch embedding method. The overlapping patch embedding method enlarges the patch window, and the input image is split into patches with overlapping. Nevertheless, this method makes the target present in two patches simultaneously, so it is impossible to reconstruct a clean background based on one patch with the target. PS-

ViT [38] and DAT [34] build deformable input embedding methods, focusing the model on complete regions. But this method will destroy the complementation between patches, breaking the principle of MECE. SwinTransformer [19] adopted a shifted windowing scheme to connect cross-window patches. However, the possibility of dividing one target into two patches is doubled with two types of shifted windows switchover. It is adverse to background reconstruction for ISTD.

3. Proposed Method

In this section, we first overview the architecture of DBR. Then we introduce the main modules: DSW, BR, and DH.

3.1. Overall Structure

The architecture of DBR can be shown in Fig. 2. Taking an infrared image as an example, if the image is directly embedded, the target will be divided into different patches. To solve this problem, in DBR, the image is first fed into DSW to calculate an offset $(\Delta x, \Delta y)$. The offset $(\Delta x, \Delta y)$ means that when the image horizontally shifts Δx pixels and vertically shifts Δy pixels, the target moves to the center of a patch instead of being divided into different patches. In the background reconstruction phase, after input embedding, the infrared image was masked twice in a complementary way. The masking strategy is grid masking. Theoretically, the target can be obtained by subtracting the generated background from the original image. However, because the generated background is not absolutely the same as the factual background, there is inevitably a reconstruction error. To minimize the influence of the reconstruction error on detection performance, finally, the original image, the generated background, and their difference are concatenated and fed into DH.

3.2. Dynamic Shift Window Module

3.2.1 Start from Single-Target

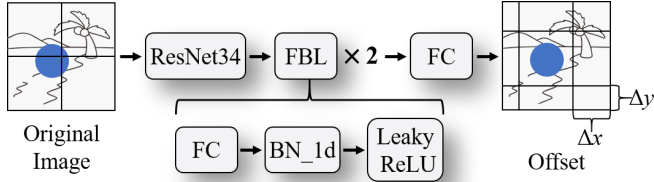


Figure 3. The structure of the dynamic shift window module (DSW). The blue circle represents the target, and the sketch represents the background.

The structure of DSW can be shown in Fig. 3. To distinguish the target and the background, in Fig. 3, Fig. 6, and Fig. 7, the blue circle represents the target, and the sketch represents the background. DSW adopts ResNet34 as the backbone and three fully-connected layers as the head. Given an infrared images X , the backbone $\mathcal{B}(\cdot)$, and head $\mathcal{H}(\cdot)$, the offset vector $[\Delta x, \Delta y]$ can be obtained by:

$$[\Delta x, \Delta y] = \mathcal{H}(\mathcal{B}(X)), \quad (1)$$

where $\Delta x, \Delta y \in \mathbb{R}^{16}$, indicates the probability of pixels the target should move horizontally or vertically within a patch (patch size is 16).

In the test phase, the offset can be obtained by:

$$\Delta x, \Delta y = (24 - \operatorname{argmax}([\Delta x, \Delta y])) \% 16, \quad (2)$$

where $\operatorname{argmax}([\Delta x, \Delta y])$ is the target center.

In the training phase, DSW treats the offset calculation as a fitting task. For any target, the distance from the target to its nearest patch center is (cx, cy) . The distance vector (cx, cy) can be obtained by rounding to the nearest integer and one-hot encoding:

$$cx, cy = \operatorname{onehot}(\operatorname{round}(cx, cy)). \quad (3)$$

DSW fits the distance vector and the offset vector with MSE loss. The specific process of generating distance vector can be shown in Alg. 1.

Since the center vector is directional, i.e., the closer the target is to the center, the better the effect of avoiding one target into two patches is. Therefore, we improve one-hot encoding by adding directional information. The difference between the proposed encoding and one-hot encoding can be shown in Fig. 4.

3.2.2 Extension to Multi-Targets

For multi-targets in one image, shifting the infrared image cannot guarantee all target centers are close to their patch

Algorithm 1 The distance vector generation for a single target.

Input: The binary image: $X_{gt} \in \mathbb{R}^{208 \times 208}$.

Output: The distance vector: (cx, cy) .

1: Obtain the target center (x, y) :

$$(x, y) = \operatorname{cv.findcounters}(X_{gt}),$$

where $\operatorname{cv.findcounters}$ is the function finding white objects from a black background in OpenCV;

2: Calculate the distance from the target to its nearest patch center:

$$(cx, cy) = (8 - x \% 16, 8 - y \% 16),$$

where “%” means modulo operation;

3: Obtain the distance vector:

$$(cx, cy) = \operatorname{onehot}(\operatorname{round}(cx, cy)).$$

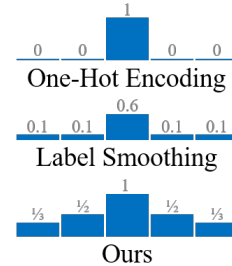


Figure 4. The difference between one-hot encoding, label smoothing, and ours.

centers. However, our purpose is to avoid dividing one target into different patches, if all targets are located in different but single patches, whether all target centers are close to their patch centers is not essential. So we change to another criterion which is shifting the infrared image to make sure target centers are far from their path edges.

Compared with DSW for a single target, in the training phase, DSW also fits the distance vector and the offset vector with MSE loss. But the process of generating distance vector is quite different: for there are more than one target, multiple distance vectors can be generated. the process of generating distance vector for multi-targets averages and weights all distance vectors according to their target radius, which can be shown in Alg. 2, Step 3 ~ 5.

In the test phase, the offset can be obtained by:

$$\Delta x, \Delta y = 16 - \operatorname{argmin}([\Delta x, \Delta y]), \quad (4)$$

where $\operatorname{argmin}([\Delta x, \Delta y])$ is the pixel that is the farthest from the target centers. That means for multi-targets, DSW maximizes the distance between target centers and patch edges. The difference between the DSW of a single target and multiple targets can be intuitively shown in Fig. 5. It is

Algorithm 2 The distance vector generation for multi-targets.

Input: The binary image: $X_{gt} \in \mathbb{R}^{208 \times 208}$.

Output: The distance vector: $(c\mathbf{x}, c\mathbf{y})$.

1: Obtain the target centers (x_i, y_i) and their radius r_i :

$$(x_i, y_i), r_i = \text{cv.findcounters}(X_{gt}), i = 1, 2, \dots, n,$$

where `cv.findcounters` is the function finding white objects from a black background in OpenCV;

2: Calculate the distance from the target to its nearest patch center:

$$(c x_i, c y_i) = (8 - x_i \% 16, 8 - y_i \% 16),$$

where “%” means modulo operation;

3: **for** i in $[1, 2, \dots, n]$ **do**

4: Obtain the distance vectors:

$$(c\mathbf{x}_i, c\mathbf{y}_i) = \text{onehot}(\text{round}(c x_i, c y_i)).$$

5: Average and weight all distance vectors:

$$(c\mathbf{x}, c\mathbf{y}) = \frac{\sum((c\mathbf{x}_i, c\mathbf{y}_i) \times r_i)}{\sum(r_i)};$$

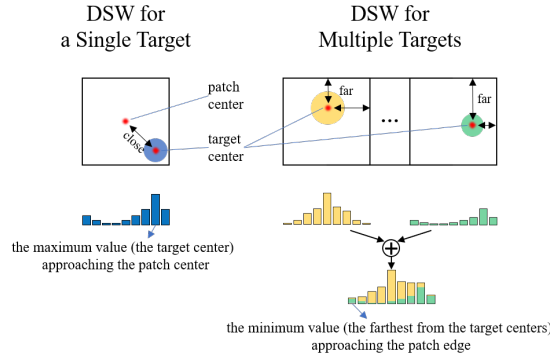


Figure 5. The difference between DSW for a single target and multiple targets.

worth noting that when there is only one target in an infrared image, the target center being far from the path edges is equivalent to the target center being close to the patch center. So there is no need to determine the number of targets in the test image, we directly use DSW for multiple targets (as shown in Fig. 5).

3.3. Background Reconstruction Module

The structure of BR can be shown in Fig. 6. Since the image needs to be shifted, the down and right parts of the image will be separately shifted to the top and left, which makes the continuous image disconnected, resulting in significant differences between the two sides of the

boundary. To deal with this problem, the infrared image is first padded to ensure no boundary after shifting. The image is then shifted according to the offset calculated by DSW, moving the target to the center of the patch. After that, the infrared image is masked twice with the grid masking strategy. The masking ratio is 50%. The two masked images are complementary. In other words, they satisfy the principle of MECE. After masking, MAE reconstructs the masked part. Finally, the background of the original image size can be generated by cropping according to the offset calculated by DSW. Given an original image $X_{ori} \in \mathbb{R}^{208 \times 208}$, the algorithm for reconstructing its background can be shown in Alg. 3.

Algorithm 3 Background reconstruction.

Input: The original image: $X_{ori} \in \mathbb{R}^{208 \times 208}$;

the offset: $(\Delta x, \Delta y)$.

Output: The generated background: $X_{gen} \in \mathbb{R}^{208 \times 208}$.

- 1: Pad the left and top regions of X_{ori} with a width of 16 pixels to the right and bottom: $X_{ori} \rightarrow X_{ori}^* \in \mathbb{R}^{224 \times 224}$;
 - 2: Horizontally shift the padded image X_{ori}^* by Δx pixels, and vertically shift by Δy pixels;
 - 3: Embed X_{ori}^* to the feature: $X_{ori}^* \rightarrow F_{ori} \in \mathbb{R}^{B \times P \times C}$;
 - 4: Complementarily grid-mask F_{ori} twice with a masking ratio of 50%: $F_{ori} \rightarrow (F_1, F_2), F_i \in \mathbb{R}^{B \times P \times \frac{C}{2}}, F_1 \cup F_2 = F_{ori}$;
 - 5: **for** F_i in (F_1, F_2) **do**
 - 6: Reconstruct F_i by MAE [12]: $F_i \rightarrow F_i^C \in \mathbb{R}^{B \times P \times \frac{C}{2}}$;
 - 7: Combine the reconstructed patch to generate the background: $F_{gen} = F_1^C \cup F_2^C$;
 - 8: De-embed the feature to the image: $F_{gen} \rightarrow X_{gen}^* \in \mathbb{R}^{224 \times 224}$;
 - 9: Crop the image to get the generated background: $X_{gen} = X_{gen}^*[\Delta x : \Delta x + 208, \Delta y : \Delta y + 208]$.
-

3.4. Detection Head

The structure of DH can be shown in Fig. 7. Because the generated background is not absolutely the same as the factual background, there is inevitably a reconstruction error. The purpose of DH is to reduce the influence of the reconstruction error on detection performance. Inspired by CourtNet [23], DH utilizes a densely connected transformer structure consisting of 12 blocks. Consider an original image $X_{ori} \in \mathbb{R}^{B \times 1 \times H \times W}$ and a generated background $X_{gen} \in \mathbb{R}^{B \times 1 \times H \times W}$, the batch size is B . Each image has one gray channel, and its width and height are W and H , respectively. First, X_{ori} , X_{gen} , and their difference are concatenated and encoded to the feature $F \in \mathbb{R}^{B \times P \times C}$, where $P = p \times p$, $C = \frac{H}{p} \times \frac{W}{p} \times c$.

Then the feature F goes through 12 blocks to get the outputs $Y \in \mathbb{R}^{B \times 1 \times H \times W}$, which are binary maps with 0 and 1 indicating whether each pixel is a target. Suppose the input of the i -th block is $F_{i-1} \in \mathbb{R}^{B \times P \times C_{i-1}}$, the output is $\mathcal{F}(F_{i-1}) \in \mathbb{R}^{B \times P \times 32}$. Then the input feature and output

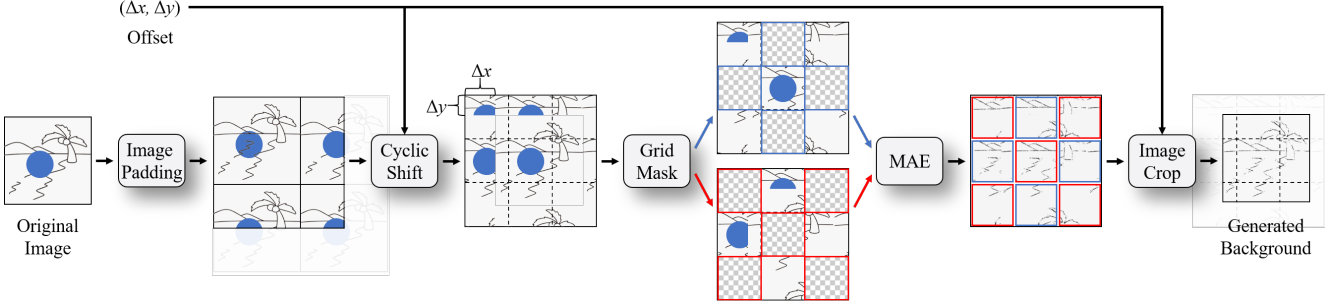


Figure 6. The structure of the background reconstruction module (BR).

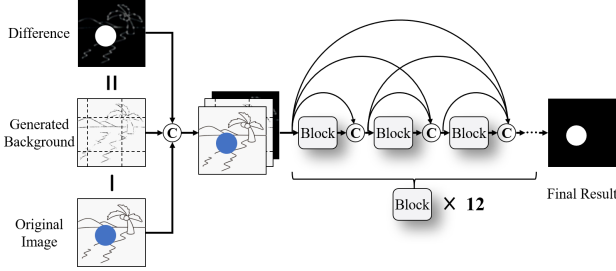


Figure 7. The structure of the detection head (DH).

feature are concatenated:

$$F_i = \text{concat}(F_{i-1}, \mathcal{F}(F_{i-1})) \in \mathbb{R}^{B \times P \times C_i}, \quad (5)$$

where $C_i = C_{i-1} + 32$. For ViT, the input feature dimension of each block is equal to the output feature dimension, and the input feature is not preserved. The output feature dimension of our block is 32. The input feature is concatenated with the output feature. The advantage of concatenation is to 1) reduce the amount of computation and increase the detection speed; 2) preserve generated backgrounds, so that the detector can take full advantage of the background-reconstruction-based method.

Since the difference of X_{ori} and X_{gen} contains targets (TP) and reconstruction error (FP), DH is prone to have a high recall rate and a low precision rate. To balance the precision and recall rates, inspired by Generalised Dice Loss [28], we propose a weighted dice loss (WDLoss). Given the result of DH as Y and the ground truth as \hat{Y} , WDLoss can be obtained by:

$$\mathcal{L}_{\text{WDL}} = -\log\left(\frac{2\gamma\Sigma(Y \times \hat{Y})}{\Sigma(Y) + \gamma\Sigma(\hat{Y})}\right), \quad (6)$$

where γ means the weighting factor. When $\gamma > 1$, the recall rate is greater than the precision rate, while $0 < \gamma < 1$, the precision rate is greater than the recall rate, here we set $\gamma = 2e - 3$.

4. Experiments

We train and test DBR on the PyTorch platform with I7-10700K CPU and RTX TITAN GPU. We use two ISTD datasets, MFIRST [30] and SIRST [5], to train and evaluate DBR. MFIRST contains 9900 training images and 100 test images, and SIRST contains 341 training images and 86 test images. For training settings, we utilize Adam and warm-up to train DBR. The warm-up steps are 200, the beginning learning rate is $4e-5$, the max learning rate is $2.5e-4$, and the number of epochs is 150. More detail can be referred to <https://github.com/PengJingchao/DBR>.

As for evaluation metrics, we use the precision rate, the recall rate, and F1-score to evaluate the binary segmentation result, which is the same as [30]. The precision rate, the recall rate, and F1-score are calculated by:

$$\text{Precision} = \frac{TP}{TP + FP}, \quad (7)$$

$$\text{Recall} = \frac{TP}{TP + FN}, \quad (8)$$

$$\text{F1-Score} = \frac{2 \times \text{Precision} \times \text{Recall}}{\text{Precision} + \text{Recall}}. \quad (9)$$

Note that a high F-1 score indicates good performance rather than only achieving high precision or recall rates [30].

4.1. The Precision of DSW

The precision of DSW is crucial for background reconstruction, for if DSW cannot find the real target centers, offsets may be wrong, resulting in dividing one target into different patches. To this end, we calculate the precision rate under the different thresholds. The results can be shown in Fig. 8. From the figure, we can find that 1) all target centers can be located within 8 pixels; 2) DSW can find target centers within 5 pixels with a precision rate of 75%. Considering the small target size (9×9) and patch size (16×16), this result is acceptable.

However, good performance does not mean that using DSW alone can satisfy the ISTD problem. We change a head of DSW that uses an upsampling layer and a 1×1

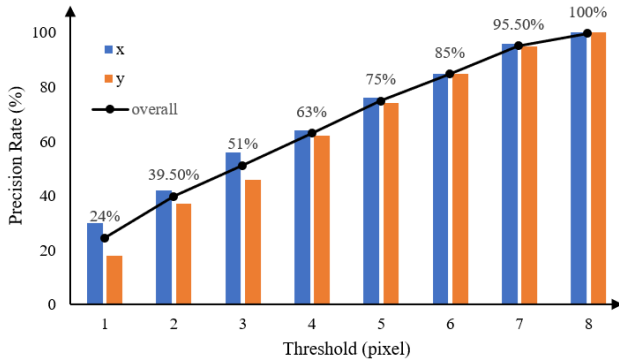


Figure 8. The precision rate of DSW under different thresholds.

convolutional layer to directly detect targets, i.e., output binary maps whose size is equal to the size of original infrared images, with “1” representing the pixel belonging to targets and “0” representing the target belonging to backgrounds. The results can be shown in the first line of Tab. 1 (DBR_v0). Using DSW alone to detect targets, F1-score is only 23.88%, which is lower compared with our DBR (64.10%). This is because the final purpose of ISTD is to determine whether each pixel belongs to the target, in other words, ISTD is a pixel-to-pixel task. Due to the resolution of the feature map of DSW is gradually decrease, DSW is not suitable to pixel-to-pixel tasks.

4.2. MAE Promotes Performance under Complex Backgrounds

In traditional ISTD methods, background reconstruction, background modeling, or background estimation belong to the same kind of technology, which has long been studied by scholars and belongs to a relatively classical technology. From the information theory, the ideal feature extractor decomposes the image information $H(\text{Image})$ consists of two parts [13]:

$$H(\text{Image}) = H(\text{Innovation}) + H(\text{Prior Knowledge}), \quad (10)$$

where $H(\text{Innovation})$ denotes the novelty part, say small targets to be detected; and $H(\text{Prior Knowledge})$ is the redundant information, say backgrounds which should be suppressed by background-reconstruction-based methods.

The background-reconstruction-based methods had been proven effective for small target detection when the detector is stationary or the background is simple. On the contrary, if the background is complex and the clutter interference is serious, traditional background-reconstruction-based ISTD methods would fail. That is because when the background is complex, the information of the background does not only in $H(\text{Prior Knowledge})$, but also in $H(\text{Innovation})$,

resulting in the target in $H(\text{Innovation})$ cannot be distinguished from the background.

Deep-learning-based methods, however, have strong representation abilities, which can encode background information into $H(\text{Prior Knowledge})$ as much as possible. And $H(\text{Innovation})$ only contains target information, so the targets can be distinguished from backgrounds. To this end, we select several infrared images with complex backgrounds and plot the spectral residual (SR) saliency maps of original images and generated backgrounds, as shown in Fig. 9. From the figure, we can find that in the original images, not only targets but also parts of backgrounds are prominent. Directly using original images cannot distinguish targets from backgrounds. But in the backgrounds generated by MAE, SR saliency maps are quite smooth and small compared with that of original infrared images, which is beneficial to the ISTD problem.

4.3. Ablation Study

Table 1. Ablation study on the MFIRST dataset. “✓” indicates using the corresponding module, while “×” indicates not.

Methods	DSW	BR	DH	Precision	Recall	F1	Flops (GMac)	Params (M)	FPS
DBR_v0	✓	×	×	15.91	80.41	23.88	3.26	21.62	76.94
DBR_v1	×	✓	×	27.72	32.53	20.91	70.30	329.24	26.39
DBR_v2	✓	✓	×	36.34	34.78	25.34	73.56	350.86	23.42
DBR_v3	×	×	✓	57.37	70.71	58.66	5.61	34.26	55.56
DBR_v4	×	✓	✓	62.04	71.10	62.63	75.91	363.50	21.69
DBR	✓	✓	✓	63.79	72.24	64.10	79.17	385.12	19.96

In order to demonstrate the effectiveness of our major modules, we implement three variations, separately pruning DSW, BR, or DH. The comparison results on MFIRST dataset are shown in Tab. 1. Among them, DSW cannot exist with DH, so we excluded this method in Tab. 1.

Compared DBR_v1 with DBR_v2, DSW improves F1-score by 4.43%, compared DBR_v4 with DBR, DSW improves F1-score by 1.47%. This is because, without DSW, BR is prone to divide one target into different patches, resulting in background reconstruction failure, which affects the detection performance. To visually demonstrate the impact of DSW on background reconstruction performance, we separately generate backgrounds with DSW and without DSW, as shown in Fig. 10. When the target is divided into different patches, directly reconstructing backgrounds will lead to targets also being reconstructed (the second column). With DSW, the target can be divided into one patch. Due to targets do not belong to backgrounds, targets cannot be reconstructed (the last column).

Compared DBR_v3 with DBR_v4, BR improves F1-score by 3.97%, which means that BR can improve detection performance under complex backgrounds. Small and dim infrared targets are difficult to distinguish from

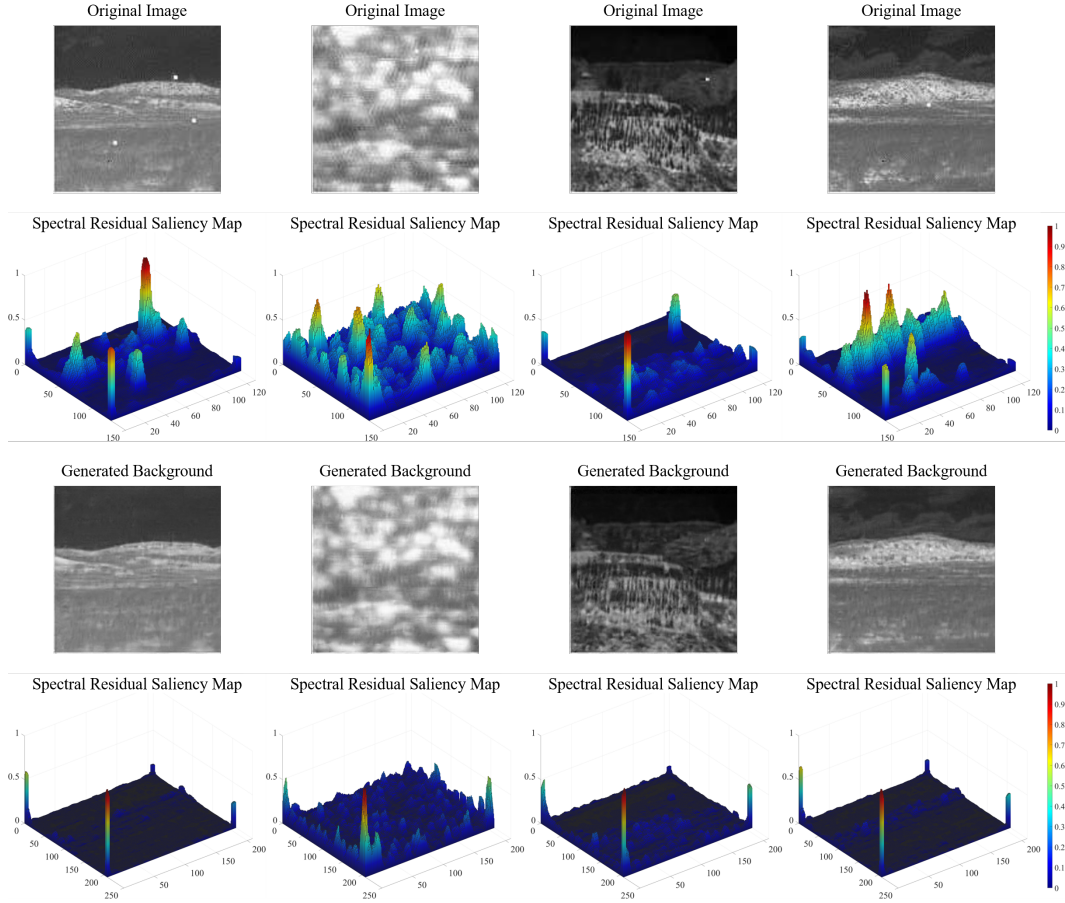


Figure 9. The spectral residual saliency maps of original infrared images and generated backgrounds.

backgrounds under complex backgrounds. With BR, targets can be easily distinguished by the difference between original images and generated backgrounds.

Compared DBR_v2 with DBR, DH improves F1-score by 38.76%. This is because the generated background is not absolutely the same as the factual background. If the differences between original images and generated backgrounds are directly used as results, the detector will regard reconstruction errors as targets, reducing the detection performance. Our proposed DBR achieves the best F1-score of 64.10%, which means that the combination of DSW, BR, and DH can achieve the best detection performance.

As for computational cost, DSW and DH have 4.12% and 7.09% of all Flops; 5.61% and 8.90% of all Params, respectively. Thus most of the computational cost comes from BR. This is because Considering the reconstruction quality will seriously affect the detection performance; simple and small reconstruction models will lead to significant reconstruction errors. Therefore, we utilize a mature but large Vision Transformer (MAE-ViT-large

[12]) for background reconstruction. Given the best performance of DBR and the detection speed (19.96 FPS), this computational cost is acceptable.

4.4. Comparison with Other Methods

We compare DBR with traditional methods (WSLCM [11], TLLCM [10], ADMD [22], MSPCM [21], and AADCDD [1]) and DL-based methods (MDvsFA-cGAN [30], ALCNet [6], ACM [5], DNANet [17], CourtNet [23], and IAANet [31]). Wang et al. [30] emphasize that F-measure indicates good performance rather than only achieving high precision or recall rates. DBR gets the best results for F1-score in two datasets over other methods, as shown in Tab. 2. In specific, DBR achieves 64.10% and 75.01% for F1-score, which is 0.2% and 1.75% higher than the second-best method (IAANet). Among DL-based methods, DBR has the closest precision rate and recall rate, indicating the effectiveness of the proposed weighted dice loss in balancing the precision rate and the recall rate.

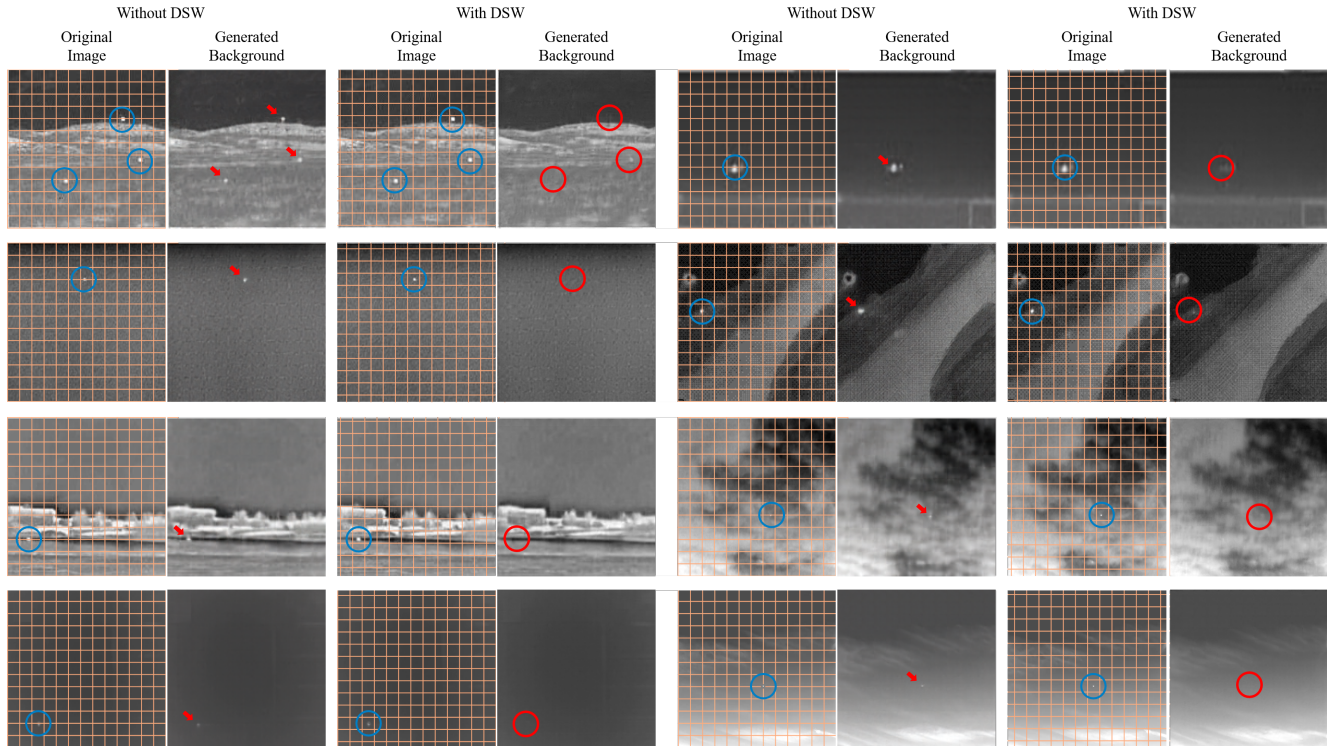


Figure 10. The performance comparison of background generation without DSW and with DSW.

Table 2. Comparison of different methods which were evaluated on MFIRST and SIRST.

Methods	MFIRST			SIRST		
	Precision	Recall	F1	Precision	Recall	F1
ADMD [22]	40.75	44.21	35.77	57.09	69.03	54.35
MSPCM [21]	49.23	49.36	39.07	69.17	69.23	62.80
AADCDD [1]	50.16	56.19	42.12	78.94	62.63	64.04
TLLCM [10]	57.70	46.11	45.15	78.19	59.08	61.18
WSLCM [11]	68.66	61.40	58.08	74.86	71.89	66.72
MDvsFA-cGAN [30]	66.00	54.00	60.00	-	-	-
ALCNet [6]	-	-	-	77.98	69.02	69.97
ACM [5]	-	-	-	67.09	85.02	66.76
DNANet [17]	56.82	70.83	57.89	61.43	90.67	70.99
CourtNet [23]	60.87	72.61	61.80	69.60	83.33	72.81
IAANet [31]	60.60	81.78	63.90	69.25	87.98	73.26
DBR (Ours)	63.80	72.24	64.10	80.70	74.09	75.01

4.5. Qualitative Performances

In order to illustrate the detection performance of DBR, as well as whether BR could generate clean backgrounds, we select 10 samples from MFIRST for comparison. Fig. 11 shows infrared images (the first column), generated backgrounds (the second column), their differences (the third column), final results (the fourth column), and ground truth (the last column).

In the first column, targets in the original infrared images are dim and small, which is difficult to distinguish from the complex backgrounds. In the second column, BR can generate clean backgrounds without targets. In the differences between the original images and generated backgrounds (the third column), the target is more apparent than in the original images, which means that background reconstruction benefits the ISTD task. However, there are lots of noises in images of the third column caused by

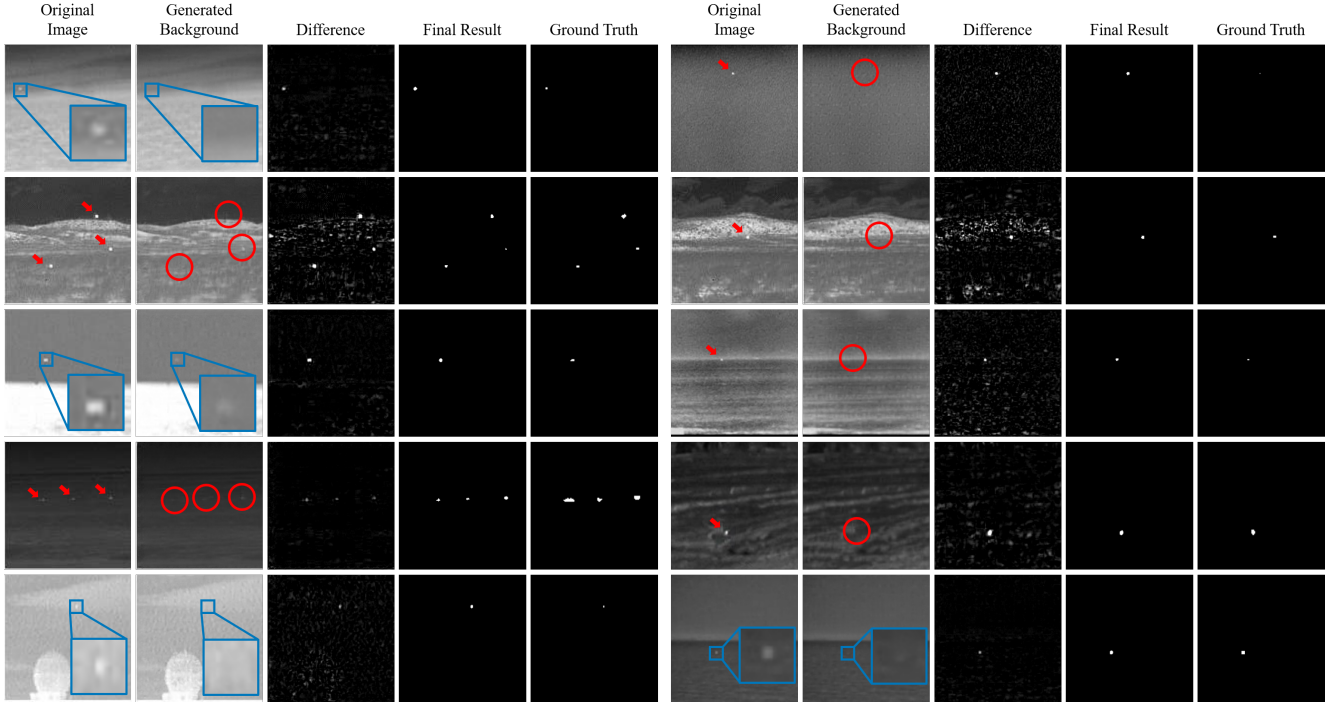


Figure 11. Qualitative performances of DBR.

reconstruction errors, so the third column cannot be directly used as the detection result. DH filters these noises, which demonstrates the effectiveness of reducing the impact of reconstruction errors on detection performance.

Based on all the experiments performed in this section, we conclude that:

1. Compared with the existing ISTD methods (WSLCM [11], TLLCM [10], ADMD [22], MSPCM [21], and AADCDD [1], MDvsFA-cGAN [30], ALCNet [6], ACM [5], DNANet [17], CourtNet [23], and IAANet [31]), DBR achieves the best F1-score on the two ISTD datasets, MFIRST (64.10%) and SIRST (75.01%), and its speed is 19.96 FPS.
2. BR can generate clean backgrounds without targets. The performance of the detector with BR is better than that of the detector without BR. Background reconstruction benefits ISTD.
3. With the consideration of dynamically shifting windows, DSW can avoid dividing one target into two patches. DSW benefits background reconstruction.
4. DH can filter noises in the differences between original images and generated backgrounds. DH makes the detector robust to reconstruction errors.

5. Conclusion

In this paper, we detect infrared small targets under complex backgrounds by background reconstruction. We propose a novel ISTD method called Dynamic Background Reconstruction (DBR). The principle of DBR is that targets can be detected through infrared images with targets minus clean backgrounds without targets. To this end, we propose a background reconstruction module (BR) based on Transformer (MAE). BR reconstructs twice grid-masked images with a masking ratio of 50%.

If one target was divided into two neighboring patches, BR would fail to reconstruct a clean background. To solve this problem, we propose a dynamic shift window module (DSW). DSW calculates offsets with that infrared images dynamically shift before input embedding. So that can prevent DBR divide one target into different patches.

In order to reduce the influence of reconstruction error on detection performance, we propose a detection head (DH) and a weighted dice loss (WDLoss). DH utilizes a structure of the densely connected Transformer. Original images, generated backgrounds, and their differences are fed into DH to get the final results. In the training phase, WDLoss balances the precision and recall rates. Extensive experiments and ablation studies demonstrate the effectiveness of the proposed main modules.

In the future, we will design a dedicated background reconstructor for ISTD. We will design the reconstructor as

a “plug-and-play” module and try integrating BR into other ISTD methods to improve the detection performance.

References

- [1] Saeid Aghaziyarati, Saed Moradi, and Hasan Talebi. Small infrared target detection using absolute average difference weighted by cumulative directional derivatives. *Infrared Physics & Technology*, 101:78–87, 2019. [3](#), [8](#), [9](#), [10](#)
- [2] Zhaoyang Cao, Xuan Kong, and Guanghui Wang. False alarm sources detection based on LNIP and local probability distribution in infrared image. In Zhigeng Pan and Xinhong Hei, editors, *Twelfth International Conference on Graphics and Image Processing (ICGIP 2020)*, volume 11720, pages 1 – 10. International Society for Optics and Photonics, SPIE, 2021. [1](#)
- [3] Philip B. Chapple, Derek C. Bertilone, Robert S. Caprari, Steven Angeli, and Garry N. Newsam. Target detection in infrared and SAR terrain images using a non-Gaussian stochastic model. In Wendell R. Watkins, Dieter Clement, and William R. Reynolds, editors, *Targets and Backgrounds: Characterization and Representation V*, volume 3699, pages 122 – 132. International Society for Optics and Photonics, SPIE, 1999. [1](#)
- [4] C. L. Philip Chen, Hong Li, Yantao Wei, Tian Xia, and Yuan Yan Tang. A local contrast method for small infrared target detection. *IEEE Transactions on Geoscience and Remote Sensing*, 52(1):574–581, 2014. [1](#), [3](#)
- [5] Yimian Dai, Yiquan Wu, Fei Zhou, and Kobus Barnard. Asymmetric contextual modulation for infrared small target detection. In *2021 IEEE Winter Conference on Applications of Computer Vision (WACV)*, pages 949–958, 2021. [1](#), [3](#), [6](#), [8](#), [9](#), [10](#)
- [6] Yimian Dai, Yiquan Wu, Fei Zhou, and Kobus Barnard. Attentional local contrast networks for infrared small target detection. *IEEE Transactions on Geoscience and Remote Sensing*, 59(11):9813–9824, 2021. [3](#), [8](#), [9](#), [10](#)
- [7] Lianghui Ding, Xin Xu, Yuan Cao, Guangtao Zhai, Feng Yang, and Liang Qian. Detection and tracking of infrared small target by jointly using ssd and pipeline filter. *Digital Signal Processing*, 110:102949, 2021. [2](#)
- [8] Alexey Dosovitskiy, Lucas Beyer, Alexander Kolesnikov, Dirk Weissenborn, Xiaohua Zhai, Thomas Unterthiner, Mostafa Dehghani, Matthias Minderer, Georg Heigold, Sylvain Gelly, Jakob Uszkoreit, and Neil Houlsby. An image is worth 16x16 words: Transformers for image recognition at scale. In *International Conference on Learning Representations*, 2021. [2](#)
- [9] Jinhui Han, Yong Ma, Bo Zhou, Fan Fan, Kun Liang, and Yu Fang. A robust infrared small target detection algorithm based on human visual system. *IEEE Geoscience and Remote Sensing Letters*, 11(12):2168–2172, 2014. [1](#)
- [10] Jinhui Han, Saed Moradi, Iman Faramarzi, Chengyin Liu, Honghui Zhang, and Qian Zhao. A local contrast method for infrared small-target detection utilizing a tri-layer window. *IEEE Geoscience and Remote Sensing Letters*, 17(10):1822–1826, 2020. [1](#), [8](#), [9](#), [10](#)
- [11] Jinhui Han, Saed Moradi, Iman Faramarzi, Honghui Zhang, Qian Zhao, Xiaojian Zhang, and Nan Li. Infrared small target detection based on the weighted strengthened local contrast measure. *IEEE Geoscience and Remote Sensing Letters*, 18(9):1670–1674, 2021. [1](#), [3](#), [8](#), [9](#), [10](#)
- [12] Kaiming He, Xinlei Chen, Saining Xie, Yanghao Li, Piotr Dollár, and Ross Girshick. Masked autoencoders are scalable vision learners. In *2022 IEEE Conference on Computer Vision and Pattern Recognition (CVPR)*, pages 16000–16009, 2022. [2](#), [3](#), [5](#), [8](#)
- [13] Xiaodi Hou and Liqing Zhang. Saliency detection: A spectral residual approach. In *2007 IEEE Conference on Computer Vision and Pattern Recognition*, pages 1–8, 2007. [7](#)
- [14] Lian Huang, Shaosheng Dai, Tao Huang, Xiangkang Huang, and Haining Wang. Infrared small target segmentation with multiscale feature representation. *Infrared Physics & Technology*, 116:103755, 2021. [2](#)
- [15] Liangjie Jia, Peng Rao, Yuke Zhang, Yueqi Su, and Xin Chen. Low-snr infrared point target detection and tracking via saliency-guided double-stage particle filter. *Sensors*, 22(7), 2022. [1](#)
- [16] Moran Ju, Jiangning Luo, Guangqi Liu, and Haibo Luo. Istdet: An efficient end-to-end neural network for infrared small target detection. *Infrared Physics & Technology*, 114:103659, 2021. [1](#)
- [17] Boyang Li, Chao Xiao, Longguang Wang, Yingqian Wang, Zaiping Lin, Miao Li, Wei An, and Yulan Guo. Dense nested attention network for infrared small target detection. *IEEE Transactions on Image Processing*, pages 1–1, 2022. [1](#), [3](#), [8](#), [9](#), [10](#)
- [18] Chang Liu, Fengying Xie, Xiaomeng Dong, Hongxia Gao, and Haopeng Zhang. Small target detection from infrared remote sensing images using local adaptive thresholding. *IEEE Journal of Selected Topics in Applied Earth Observations and Remote Sensing*, 15:1941–1952, 2022. [1](#)
- [19] Ze Liu, Yutong Lin, Yue Cao, Han Hu, Yixuan Wei, Zheng Zhang, Stephen Lin, and Baining Guo. Swin transformer: Hierarchical vision transformer using shifted windows. In *Proceedings of the IEEE/CVF International Conference on Computer Vision (ICCV)*, 2021. [2](#), [3](#)
- [20] Deyong Lu, Qiang Ling, Yuanyuan Zhang, Zaiping Lin, and Wei An. Iistd: Image inpainting-based small target detection in a single infrared image. *IEEE Journal of Selected Topics in Applied Earth Observations and Remote Sensing*, 15:7076–7087, 2022. [2](#)
- [21] Saed Moradi, Payman Moallem, and Mohamad Farzan Sabahi. A false-alarm aware methodology to develop robust and efficient multi-scale infrared small target detection algorithm. *Infrared Physics & Technology*, 89:387–397, 2018. [8](#), [9](#), [10](#)
- [22] Saed Moradi, Payman Moallem, and Mohamad Farzan Sabahi. Fast and robust small infrared target detection using absolute directional mean difference algorithm. *Signal Processing*, 177:107727, 2020. [3](#), [8](#), [9](#), [10](#)

- [23] Jingchao Peng, Haitao Zhao, Zhengwei Hu, Kaijie Zhao, and Zhongze Wang. Courtnet for infrared small-target detection. *arXiv*, 2209.13780, 2022. [3](#), [5](#), [8](#), [9](#), [10](#)
- [24] Junhwan Ryu and Sungho Kim. Heterogeneous gray-temperature fusion-based deep learning architecture for far infrared small target detection. *Journal of Sensors*, 2019:4658068, Aug 2019. [1](#)
- [25] Manish Sharma, Mayur Dhanaraj, Srivallabha Karnam, Dimitris G. Chachlakis, Raymond Ptucha, Panos P. Markopoulos, and Eli Saber. Yolors: Object detection in multimodal remote sensing imagery. *IEEE Journal of Selected Topics in Applied Earth Observations and Remote Sensing*, 14:1497–1508, 2021. [1](#)
- [26] Lars Sommer and Arne Schumann. Deep learning-based drone detection in infrared imagery with limited training data. In Henri Bouma, Radhakrishna Prabhu, Robert James Stokes, and Yitzhak Yitzhaky, editors, *Counterterrorism, Crime Fighting, Forensics, and Surveillance Technologies IV*, volume 11542, pages 1 – 12. International Society for Optics and Photonics, SPIE, 2020. [2](#)
- [27] Zizhuang Song, Jiawei Yang, Dongfang Zhang, Shiqiang Wang, and Zheng Li. Semi-supervised dim and small infrared ship detection network based on haar wavelet. *IEEE Access*, 9:29686–29695, 2021. [1](#)
- [28] Carole H. Sudre, Wenqi Li, Tom Vercauteren, Sebastien Ourselin, and M. Jorge Cardoso. Generalised dice overlap as a deep learning loss function for highly unbalanced segmentations. In *Deep Learning in Medical Image Analysis and Multimodal Learning for Clinical Decision Support*, pages 240–248. Springer International Publishing, 2017. [6](#)
- [29] Huaichao Wang, Haifeng Li, Hai Zhou, and Xinwei Chen. Low-altitude infrared small target detection based on fully convolutional regression network and graph matching. *Infrared Physics & Technology*, 115:103738, 2021. [2](#)
- [30] Huan Wang, Luping Zhou, and Lei Wang. Miss detection vs. false alarm: Adversarial learning for small object segmentation in infrared images. In *2019 IEEE/CVF International Conference on Computer Vision (ICCV)*, pages 8508–8517, 2019. [1](#), [3](#), [6](#), [8](#), [9](#), [10](#)
- [31] Kewei Wang, Shuaiyuan Du, Chengxin Liu, and Zhiguo Cao. Interior attention-aware network for infrared small target detection. *IEEE Transactions on Geoscience and Remote Sensing*, 60:1–13, 2022. [1](#), [3](#), [8](#), [9](#), [10](#)
- [32] Wenhai Wang, Enze Xie, Xiang Li, Deng-Ping Fan, Kaitao Song, Ding Liang, Tong Lu, Ping Luo, and Ling Shao. Pvtv2: Improved baselines with pyramid vision transformer. *Computational Visual Media*, 8(3):1–10, 2022. [2](#), [3](#)
- [33] Xin Wang, Guofang Lv, and Lizhong Xu. Infrared dim target detection based on visual attention. *Infrared Physics & Technology*, 55(6):513–521, 2012. [1](#)
- [34] Zhuofan Xia, Xuran Pan, Shiji Song, Li Erran Li, and Gao Huang. Vision transformer with deformable attention. In *Proceedings of the IEEE/CVF Conference on Computer Vision and Pattern Recognition (CVPR)*, pages 4794–4803, June 2022. [2](#), [3](#)
- [35] Hanyu Xiang, Qin Zou, Muhammad Ali Nawaz, Xianfeng Huang, Fan Zhang, and Hongkai Yu. Deep learning for image inpainting: A survey. *Pattern Recognition*, 134:109046, 2023. [2](#)
- [36] Dongfang Yang, Xing Liu, Hao He, and Yongfei Li. Air-to-ground multimodal object detection algorithm based on feature association learning. *International Journal of Advanced Robotic Systems*, 16(3):1729881419842995, 2019. [1](#)
- [37] Li Yuan, Yunpeng Chen, Tao Wang, Weihao Yu, Yujun Shi, Zi-Hang Jiang, Francis E.H. Tay, Jiashi Feng, and Shuicheng Yan. Tokens-to-token vit: Training vision transformers from scratch on imagenet. In *Proceedings of the IEEE/CVF International Conference on Computer Vision (ICCV)*, pages 558–567, October 2021. [2](#), [3](#)
- [38] Xiaoyu Yue, Shuyang Sun, Zhanghui Kuang, Meng Wei, Philip Torr, Wayne Zhang, and Dahua Lin. Vision transformer with progressive sampling. *Proceedings of the IEEE/CVF International Conference on Computer Vision (ICCV)*, 2021. [2](#), [3](#)
- [39] Vitjan Zavrtnik, Matej Kristan, and Danijel Skocaj. Reconstruction by inpainting for visual anomaly detection. *Pattern Recognition*, 112:107706, 2021. [2](#)
- [40] Yu Zhang, Yan Zhang, Zhiguang Shi, Jinghua Zhang, and Ming Wei. Design and training of deep cnn-based fast detector in infrared suav surveillance system. *IEEE Access*, 7:137365–137377, 2019. [2](#)
- [41] Zhaoxiang Zhang, Akira Iwasaki, Guodong Xu, and Jianing Song. Cloud detection on small satellites based on lightweight U-net and image compression. *Journal of Applied Remote Sensing*, 13(2):1 – 13, 2019. [2](#)
- [42] Mingjing Zhao, Wei Li, Lu Li, Jin Hu, Pengge Ma, and Ran Tao. Single-frame infrared small-target detection: A survey. *IEEE Geoscience and Remote Sensing Magazine*, 10(2):87–119, 2022. [1](#), [2](#)